THE JOURNAL OF PHYSICAL CHEMISTRY A
A JOURNAL OF THE AMERICAN CHEMICAL SOCIETY

pubs.acs.org/JPCA

Article

Electronic Coherences Steer the Strong Isotope Effect in the Ultrafast Jahn–Teller Structural Rearrangement of Methane Cation upon Tunnel Ionization

Published as part of The Journal of Physical Chemistry virtual special issue "125 Years of The Journal of Physical Chemistry".

Martin Blavier, Ksenia Komarova, Cayo E. M. Gonçalves, R. D. Levine, and F. Remacle*

Cite This: https://doi.org/10.1021/acs.jpca.1c06431

Read Online

ACCESS | Metrics & More | Article Recommendations | Supporting Information

ABSTRACT: We report on fully quantum electronic-nuclear dynamics following sudden ionization from the neutral in the three lowest electronic states of the CH_4^+ and CD_4^+ cations. There is a strong Jahn–Teller effect in the Franck–Condon region, and we employ two nuclear degrees of freedom that span the internal coordinates involved in the Jahn–Teller coupling. The initial state results from tunneling ionization by a strong IR field which coherently pumps the three lowest states of the cation, D_0, D_1, and D_2. The quantum dynamical simulations show that a strong isotope effect occurs when the ionization significantly accesses the D_2 state of the cation in the Franck–Condon region. The computed isotope effect is larger than expected on the basis of the effective mass ratio. The strong effect is due to fast oscillations of the electronic coherences between the D_2 and the D_1 and D_0 electronic states and their modulation by the nonadiabatic couplings before a significant onset of nuclear motion. The magnitude of the effect is similar to the one that we previously reported for a sudden photoionization process. A strong isotope effect has been observed in high harmonic spectroscopy studies of the very short time dynamics Jahn–Teller structural rearrangement of the methane cation upon sudden ionization.

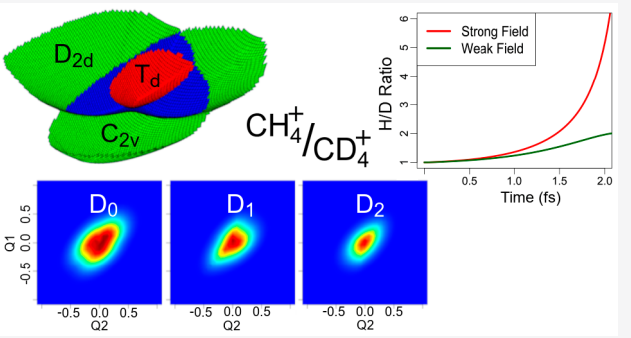

INTRODUCTION

The progress in the engineering of atto and few femtosecond optical pulses[1−6] provides access to initiating, controlling, and probing electronic coherences in molecular systems.[7−10] Electronic coherences are built upon photoexcitation or photo or tunneling ionization when several electronic states are simultaneously and coherently accessed. This is made possible by the broad energy bandwidth of short sub fs or atto pulses. The nonstationary superposition of electronic and vibrational states built by the excitation process then evolves coherently on the potentials of the different electronic states where it encounters regions of nonadiabatic couplings between electronic states that is driven by the nuclear motion. In this new intrinsically post Born and Oppenheimer regime, not only nuclei but also electrons are out of equilibrium in the initially pumped state.[10,11] The new aspect brought by the post Born–Oppenheimer regime is the formation of electronic coherences at the excitation step which modulate the temporal and spatial localization of the electronic density in the molecule. As the dynamics unfold, new electronic states and new nuclear modes are brought in by the nonadiabatic and anharmonic couplings. One of the challenges of attochemistry is to devise control schemes that exploit the electronic coherences built at the excitation step to steer the nuclei toward specific products.

A particularly interesting case for studying the role of electronic coherences built at the excitation step is when the regions of nonadiabatic coupling are localized in the Franck–Condon region or in its close vicinity. A textbook example of such a situation is the Jahn–Teller rearrangement that occurs in the methane cation upon sudden ionization of the neutral. The sudden ionization creates a superposition of those three electronic states of the cation that are degenerate at the equilibrium T_d geometry of the neutral molecule. In the cation, the T_d geometry is unstable because of the Jahn–Teller (JT) effect, which induces a structural rearrangement to a geometry of a lower symmetry. This rearrangement has been extensively

Received: July 19, 2021
Revised: October 7, 2021

Downloaded via UNIV DE LIEGE on October 22, 2021 at 15:07:31 (UTC).
See https://pubs.acs.org/sharingguidelines for options on how to legitimately share published articles.

ACS Publications
© XXXX American Chemical Society

studied experimentally by photoelectron[12,13] and electron paramagnetic resonance[14,15] spectroscopies in solid matrices and theoretically using various levels of electronic structure theory;[16−18] a review can be found in ref 19. The rearrangement is ultrafast and occurs in a few femtoseconds through strong nonadiabatic couplings between the three electronic states in the Franck−Condon region where the electronic and nuclear motions are strongly correlated. The nonadiabatic coupling involves the two t_2 and the e mode of the T_d geometry. The JT rearrangement is therefore significantly affected by isotopic substitution. A pioneering study of the first 2 fs of the dynamics by high harmonic spectroscopy indeed reports a strong isotope effect in the harmonics yields in the first half period (≈1.6 fs) of the strong ($\approx 2 \times 10^{14}$ W/cm^2) 800 nm IR laser radiation used to produce the harmonic spectra.[20,21] The ratio of the yields in harmonics of CD_4 and of CH_4 is found to vary between 1.5 at 1 fs and 3 at 1.6 fs, reaching a value larger than expected on the basis of the effective mass ratio, =1.86. This experimental result stimulated several theoretical studies.[22−26] The yield in high harmonics has been shown to be proportional to the autocorrelation function, $|C(t)|^2$, of the initial state of the cation.[27] The reason for the isotope effect is attributed to the slower motion out of the Franck−Condon region of CD_4^+ with respect to CH_4^+ which leads to a higher yield in harmonics for CD_4 when the electron recombines with the cation. Theoretical studies therefore compare the ratio of the autocorrelation of the initial state of the two isotopomers to the ratio of the yields in harmonics. Mondal and Varandas reported MCTDH computations for a quasi vibronic coupling model in the three lowest states of the methane cation with increasing nuclear dimensionality up to the full 9 dimensionality.[24−26] Their computations show that 5 nuclear degrees of freedom, the t_2 mode and the e mode of the T_d geometry that are strongly involved in the Jahn−Teller effect are necessary to account for the large experimental isotope effect observed in the first two fs of the dynamics.[25,26] In these computations, the ionization process is not described in detail, and the three electronic states are populated uniformly in the geometries of the Franck−Condon region for a fixed orientation of the molecule. Madsen[23] studied the tunneling ionization rates and their angular dependence and confirmed the involvement of the same normal modes. Patchkovskii[22] studied the role of the dependence of the early time dynamics on the gradient and the curvature of the potentials in the vicinity of the T_d point on the large value of the ratio of the autocorrelation functions of CD_4^+ and CH_4^+.

We recently reported on the isotope effect that occurs in the methane cation when the neutral is photoionized by a XUV attopulse.[28] In this previous work, we carried out a fully quantum dynamical study in the three lowest electronic states of the cation, using two nuclear coordinates described on a grid. The two coordinates span the normal modes of the molecule, with high weights on the two t_2 modes and the e mode involved in the JT distortion. The photoionization by the XUV attopulse was described by sudden ionization and the photoionization matrix elements are computed for each grid point geometry in the Franck−Condon region for an ensemble of 8000 orientations with respect to the electric field of the ionizing pulse. We considered two carrier frequencies of the XUV pulse, which allows accessing the three lowest states of the cation in different amounts. A low carrier frequency (≈13.65 eV) that corresponds to the ninth harmonic of a 800 nm IR radiation used to generate the XUV pulse leads to populations in the ground state, D_0, and in the first excited state, D_1, of the cation, with a very low amount in D_2. On the other hand, a carrier frequency that corresponds to the 11th harmonic (17.9 eV) of the 800 nm IR radiation accesses the three lowest states of the cation in roughly equal amounts. We showed by computing the ratio of the autocorrelation functions for an ensemble of randomly oriented molecules that a large isotope effect, with a ratio ≈2.6 at 1.6 fs, is obtained for a photoionization by the higher carrier frequency XUV pulse, that access the D_2 state. A lower isotope effect, with a ratio of 1.5 closer to the effective mass ratio (μ_{C-D}/μ_{C-H} = 1.86), is obtained for photoionization by the low carrier frequency XUV pulse, which does not significantly accesses the D_2 state. We further showed in ref[28] that the autocorrelation function of the initial state being an observable sensitive on electronic coherences, that the larger isotope effect has a quantum nature and is due to the short time dynamics of the electronic coherences that involve the D_2 state.

Here, we pursue our study of the role of electronic coherences in inducing large isotope effects, larger than the classical effect due to the different effective masses, by reporting fully quantal dynamical simulations following a sudden strong field tunnelling ionizing process, as is occurring in high harmonic spectroscopy. In order to assess the role of electronic coherences on the initial state that results from a strong field tunneling ionization, we consider two field strengths of the IR pulse that generates the harmonics of CH_4: a low field strength of 0.03 au (3.16×10^{13} W/cm^2) that does not significantly ionize to the D_2 state in the Franck−Condon region and a larger field strength of 0.075 au (2×10^{14} W/cm^2) that significantly ionizes the D_2 state. Our results show that as in the photoionization case, a large isotope effect of ≈2.5 on the ratio of the autocorrelation functions is obtained for the stronger pulse, when the D_2 state is populated by the ionization process.

We have previously reported similar isotope effects that arise when an electronic coherence reaches a region of nonadiabatic coupling in the diatomic molecules N_2 and LiH.[29−31] We showed using algebraic techniques for one nuclear dimension that the direction and the magnitude of the amplitude transfer when the electronic coherence reaches the coupling region is governed by the phase difference between the two electronic states present in the wave packet. The phase difference factorizes into a classical term that depends linearly on the reduced mass and a purely quantum part, which is nonlinear in the mass.[32] The presence of this quantum term explains that the isotope effect is larger than the classical one when the vibronic wave packet is made of several electronic states.

We briefly report on the computational model in section 2. We discuss the results for tunnel ionization and provide a discussion of how the electronic coherences steer the isotope effect in section 3. Conclusions are given in section 4.

2. COMPUTATIONAL DETAILS

2.1. Electronic Structure and Nuclear Grid. We use the same two coordinates and the same level of electronic structure and the same potential energy surfaces (PES) as described in ref 28. The electronic structure is computed for the geometry of each grid point at the SA(3)-CASSCF (9,8) /6-31G++(2df,2pd) using MOLPRO,[33] which provides the values of the potential energy for the three states, D_0, D_1, and D_2 as well as the nonadiabatic couplings (NAC). The computed vertical

https://doi.org/10.1021/acs.jpca.1c06431
J. Phys. Chem. A XXXX, XXX, XXX−XXX

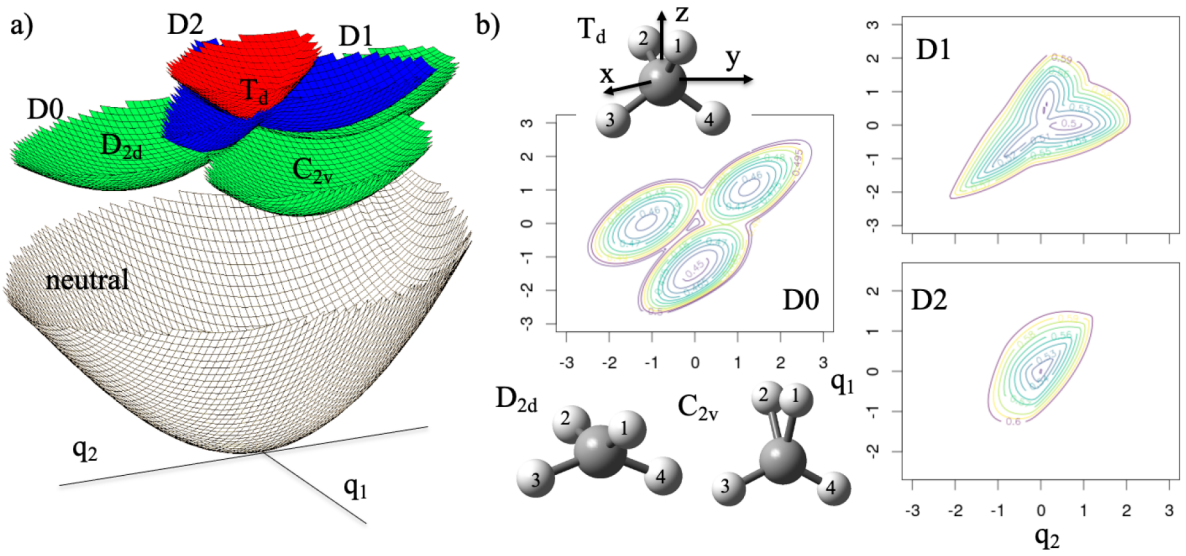

Figure 1. (a) Three-dimensional view of the PES of the three lowest states of cation, D_0, D_1, and D_2, computed at the SA-3-(9,8) /6-31G++(2df,2pd). (b) Isocontours of the PES of the D_0, D_1, and D_2 as indicated. The unstable T_d geometry and the geometries of the D_{2d} and C_{2v} minima on the D_0 grid are also shown. Their (q_1,q_2) coordinates are (0,0) for T_d, (−1.4,0) for C_{2v} and (0,−1.12) for D_{2d}. Isocontour spacing: D_0: 0.01 eV; D_1: 0.009 eV; D_2: 0.015 eV.

IP at the T_d geometry is 13.6 eV. The results of the electronic structure are in good agreement with ref 18. The larger atomic basis set allows for a good description of the tunnel ionization process.

The three lowest states of the methane cation, D_0, D_1, and D_2, are unstable at the equilibrium geometry of the neutral ground state. The two nuclear coordinates of the grid, q_1 and q_2, are designed to describe the dynamics of the JT rearrangement at short time. They are defined as linear combination of Cartesian displacements; the coefficients are reported in Table S1 of the SI. The coordinate q_1 points to the C_{2v} geometry and the coordinate q_2 to the D_{2d} one. To both, we added a small geometrical distortion in order to correctly describe the nonadiabatic coupling (NAC) so that all geometries on the grid are of C_1 symmetry. The two coordinates span the normal modes of the T_d geometry that are involved in the JT effect (the 2 t_2 and the e modes), as well as the seams between the electronic states in the Franck−Condon region, where the geometry is of lower symmetry. The values of the coefficients of the q_1 and the q_2 coordinates on the modes of the T_d geometry are reported in Table S2 of the SI. The coordinate q_1 has large coefficients on one of the t_2 modes, as well as on the e mode, with smaller coefficients on the other t_2 mode and on the a_1 mode. The q_2 coordinate has a large weight on the e mode of the T_d geometry. The two coordinates therefore describe the modes of the T_d form that are involved in the NAC coupling due to the JT effect. We include 146 point along q_1 and 184 along q_2, which leads to 26864 grid points per electronic state (see ref 28 and SI for more details on the coordinates). Figure 1b shows isocontours of the PES of D_0, D_1, and D_2 computed on the grid of the q_1 and q_2 coordinates. In CH_4, the H nuclei are equivalent. For the particular realization shown in the insets of Figure 1b, without the distortions added to q_1 and q_2 that takes the geometries of the grid points out of the C_{2v} geometry, we should have two equivalent C_{2v} minima. The distortion, which is needed to capture the NAC seams, lowers the symmetry of the C_{2v} minima. On the grid, the geometry closest to the global C_{2v} minimum falls at (q_1 = −1.4, q_2 = 0). It has a root-mean-square deviation (RMSD) of 0.0418 Bohr with respect to the C_{2v} geometry. The second C_{2v} minimum at q_1 = 1.08,q_2 = 1.26, RMSD = 0.1384 Bohr, has a more distorted geometry, closer to a C_s geometry. It is 0.158 eV higher than the lowest distorted C_{2v} minimum. On the grid, the PES also exhibits a minimum of distorted D_{2d} geometry (q_1 = 0, q_2 = −1.12, RMSD = 0.0321 Bohr) that is ≈0.165 eV above the lowest distorted C_{2v} minimum (Figure 1a). Since the coordinate q_2 has a high weight on the e mode of the Td geometry, this result is consistent with the results of ref 25, which shows that a cut of the hyperpotential energy surface along the e mode exhibits a minimum of D_{2d} geometry. In full dimensionality at the CASSCF (9,8) /6-31G++(2df,2pd) level, the D_{2d} geometry on D_0 is a saddle point, with an energy 0.28 eV above the C_{2v} minima in agreement with the results of ref 18. We also recover a saddle point of C_{3v} symmetry, at higher energy (0.44 eV) which falls outside of the grid. D_1 exhibits three minima located close to the NAC seams while D_2 has a minimum at the T_d point. The PES's of the three states have very different gradients around the T_d point. The gradient of D_0 out of the unstable T_d point is very steep but the minima around D_{2d} and C_{2v} are very shallow. D_1 is also unstable at the T_d point, the D_1 PES exhibits three minima that are located close to the NAC seams with D_0, see Figure 1b. The PES around the T_d minimum on D_2 is very steep. This implies that the wave packet transferred to D_2 by the ionization process remains localized in this tight potential which makes the NAC with the D_1 and D_0 very efficient close to the T_d geometry. However, the initial wave packets on D_1 and D_0 rapidly leave the region of the unstable T_d geometry while the D_2 wave packet is trapped around the T_d point.

The two coordinates q_1 and q_2 therefore capture the features of the potentials and the NAC couplings essential to describe the dynamics in the first dozen fs of the Jahn−Teller rearrangement. To capture the much longer time dynamics, such as the exchange between the equivalent C_{2v} minima induced by large amplitude motion that occurs on a ps time scale,[12,13,19] it is necessary to use a full dimensional description of the nuclear motion.

https://doi.org/10.1021/acs.jpca.1c06431
J. Phys. Chem. A XXXX, XXX, XXX−XXX

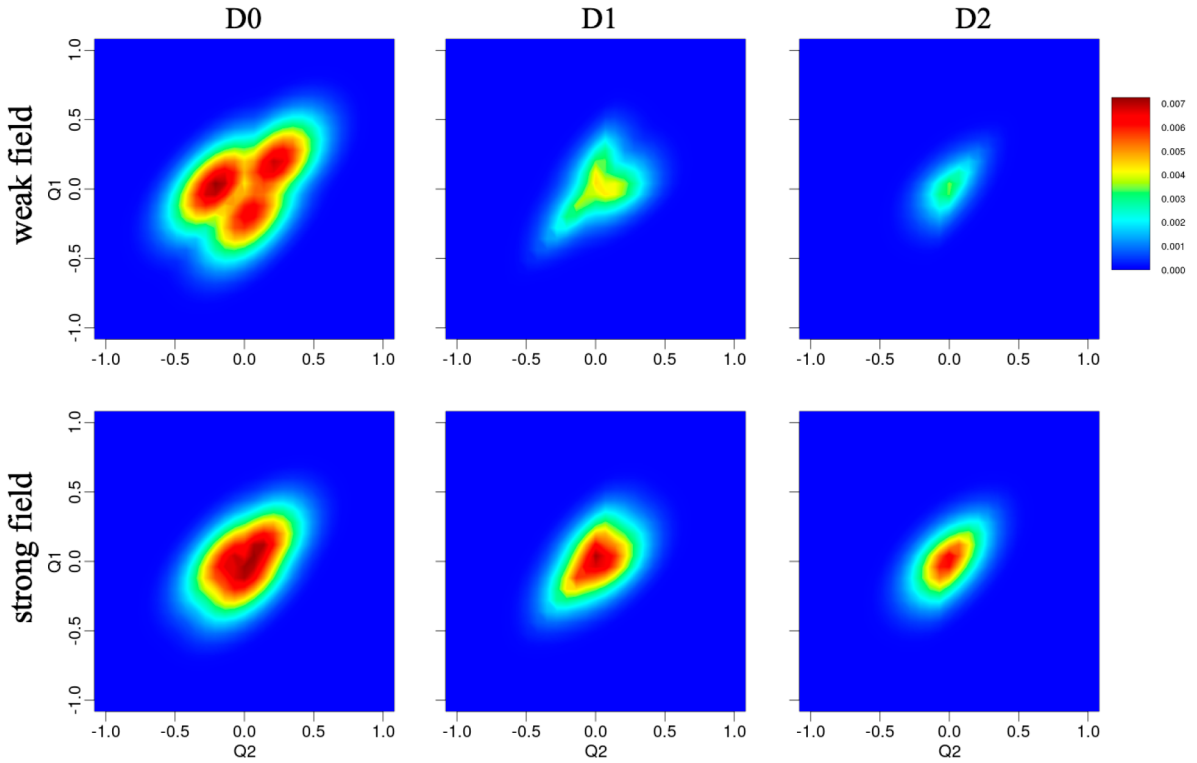

Figure 2. Localization of the initial state, $|c_{gi}|^2 = \frac{1}{N}\sum_{m=1}^{8000}|c_{gi}^m|^2$ on the three electronic states, D_0, D_1, and D_2 for CH_4^+ computed for an ensemble of 8000 random orientations on the unit sphere for the weak field strength, top row and the strong field strength, bottom row. The localization of the CD_4^+ initial states is shown in Figure S1.

2.2. Initial Amplitudes in the States of the Cation.

The tunneling amplitudes on the three states of the cation are determined within the three-step model,[34] assuming a tunneling ionization process at the maximum of the electric field for a random orientation of the molecular frame with respect to the laboratory frame. We use a MO-ADK model[35,36] for describing the tunneling ionization from the neutral ground state to a particular electronic state of the cation, D_i, and a given orientation of the electric field, $\hat{\mathbf{e}}_m$, with respect to the molecular frame at the nuclear geometry of a given grid point g. We further assume that the structure parameters that appear in the expression of the molecular asymptotic wave function closely resembles the one electron density of the active electron that is ionized.[37] The latter is given by the Dyson orbital, $\phi_{g,D_i}^{\text{Dyson}}(\mathbf{r}) = \int d\mathbf{r}_1 ... d\mathbf{r}_{N-1} \Psi_{g,D_i}^{\text{cat}}(\mathbf{r}_1 ... \mathbf{r}_{N-1}) \Psi_{g,GS}^{\text{neut}}(\mathbf{r}_1, \cdots, \mathbf{r}_N)$ with $\mathbf{r}$ the electronic coordinate and N the number of electrons of the neutral. The strong field ionization probabilities, W_{g,D_i}^m at each grid point to an electronic state of the cation D_i for a given orientation of the electric field $\hat{\mathbf{e}}_m$ are then given as the product of the norm of the Dyson MO, $N_{g,D_i} = \int d\mathbf{r} |\phi_{D_i}^{\text{Dyson}}(\mathbf{r})|^2$ multiplied by the Keldysh tunnel ionization rate

$$K_{g,D_i}^m = \exp\left(-\frac{2}{3}\frac{(2IP_{g,D_i}^m)^{3/2}}{|\mathbf{F}|}\right) \tag{1}$$

and weighted by the square modulus of the vibrational ground state wave function of the neutral at this grid point, $|c_{g,GS}^{\text{neut}}|^2$[38]

$$W_{g,D_i}^m = |c_{g,GS}^{\text{neut}}|^2 N_{g,D_i} K_{g,D_i}^m \tag{2}$$

In eq 1, $|\mathbf{F}|$ is the strength of the field. IP_{g,D_i}^m is the IP at the geometry of grid point g for a given orientation of the electric field, $\hat{\mathbf{e}}_m$, corrected by the Stark shift due to the strong electric field of the IR pulse on the neutral and on the cation.

$$IP_{g,D_i}^m = E_{g,D_i}^{\text{cat}} - E_{g,GS}^{\text{neut}} - |\mathbf{F}|\hat{\mathbf{e}}_m \cdot (\mu_{g,D_i}^{\text{cat}} - \mu_{g,GS}^{\text{neut}}) \tag{3}$$

where μ_{g,D_i}^{cat} and $\mu_{g,GS}^{\text{neut}}$ are the permanent dipoles of the cation state D_i and of the neutral at grid point g. The Dyson MO's were computed as described in ref 39 and their norm computed from their expansion in AOs. At each grid point, the amplitudes of the initial state on each electronic state of the cation, $c_{i,g}^m$'s, are proportional to the strong field ionization probabilities, W_{g,D_i}^m (eq 2) and therefore to the ionization rates, K_{g,D_i}^m (eq 1):

$$c_{g,i}^m \propto \sqrt{W_{g,D_i}^m} \tag{4}$$

We show the localization of the initial state as a heatmap in the (q_1,q_2) coordinates in Figure 2 for CH_4^+ for two values of the field strength: a low value of 0.03 au (3.16×10^{13} W/cm^2), called weak field (wf) in the following, and a higher value of 0.075 au (2×10^{14} W/cm^2), called strong field (sf) in the following. This higher value corresponds to the peak power of the IR 800 nm pulse used to measure the high harmonic yields in ref.[20] Each orientation $\hat{\mathbf{e}}_m$ defines a pure state. In a typical experiment, the orientation of the molecule is random with respect to the electric field. The results reported below are therefore computed for an ensemble of 8000 random orientations on unit sphere.

In Figure 2, one can see that for the weak field, the localization of the initial state maps the isocontours of PES

https://doi.org/10.1021/acs.jpca.1c06431
J. Phys. Chem. A XXXX, XXX, XXX−XXX

shown in Figure 1. The reason is that in the approximation we use, the dependence of the tunneling rate on the orientation comes from the Stark effect on the IP (eq 3) which for this field strength is very weak. The tunneling rate then becomes determined by the field free energy difference between the neutral ground state and the electronic state of the cation at a given grid point. Since the PES of the neutral ground state is shallow in the Franck−Condon region, the variation of the IP on the grid is given by the energies of the cation states. The Stark effect is larger on the states of the cation than on the neutral GS. Therefore, for higher field strengths, one obtains lower IP values than in the weak field case, which leads to a higher ionization yields, more initial populations in D_1 and D_2, and a more uniform localization of the initial states around the T_d point. We obtain very similar initial localization of the initial states for CD_4^+ see Figure S1 of the SI. The reason is that the only isotopic dependence of the initial state comes from the localization of the ground vibrational state of the neutral on the grid. The latter is slightly more localized around the T_d geometry for CD_4^+ than for CH_4^+.

2.3. Vibronic Hamiltonian on the Grid. On the grid, the vibronic Hamiltonian used to propagate the principal component vectors, $\mathbf{U}_s$, takes the form, see also Section S1 of the SI.

$$\mathbf{H}_{ig,jg'} = \mathbf{T}_{ig,jg'}\delta_{ij} + \mathbf{V}_{ig,jg'}\delta_{ij}\delta_{gg'} + \left(\frac{1}{i}\tau_{ig,jg}\delta_{gg'}\right).\mathbf{P}_{igjg'} \tag{5}$$

In eq 5, $\mathbf{T}$ is the kinetic energy, $\mathbf{V}$ the potential, τ the nonadiabatic coupling, and $\mathbf{P}$ the momentum. The Hamiltonian includes the NAC coupling (third term on the rhs) between each pair of electronic states. We neglect the second derivative NAC term, which is much smaller. In the NAC term (last term of eq 5), $i \neq j$.

In eq 5, the kinetic energy operator $\hat{T}$ in internal coordinates takes the form

$$\hat{T} = -\frac{1}{2}\left(\frac{1}{\mu_1}\frac{\hat{\partial}^2}{\partial q_1^2} + \frac{1}{\mu_2}\frac{\hat{\partial}^2}{\partial q_2^2} + \frac{2}{\mu_{12}}\frac{\hat{\partial}^2}{\partial q_1 \partial q_2}\right) \tag{6}$$

and the components of the nonadiabatic coupling vector, $\tau_{ig,jg'}$ are expressed in internal coordinates. The derivation and the expression of the reduced masses is given in the SI, as well as 2D maps showing the value of two components of the NAC coupling vectors, $\tau_{ig,jg}(q_1)$ and $\tau_{ig,jg}(q_2)$ on the grid for the three pairs of states. $\mathbf{P}$ is the momentum vector, whose two components are given by $\hbar/i\ \partial/\partial q_1$ and $\hbar/i\ \partial/\partial q_2$. We solve the time-dependent Schrödinger equation, $i\hbar d\mathbf{c}/dt = \mathbf{Hc}$ numerically. The vector $\mathbf{c}$ is the vector of the complex amplitudes of the time-dependent wave function, $c_{ig}(t)$, on the grid. The nonlocal kinetic energy and momentum matrix elements are computed using a finite difference algorithm (see SI). We report below the time-dependent value of the off diagonal term of the Hamiltonian averaged over grid points for each pair of electronic states:

$$H_{ij}(t) = \sum_g c_{ig}{}^*(t)\left(\frac{1}{i}\right)\tau_{ig,jg}\hat{P}\sum_{g'} c_{jg'}(t) \tag{7}$$

2.4. Quantum Dynamics on the Grid Averaged over Random Orientations. We report below results of the quantum dynamics averaged over 8000 random orientations of the electric field with respect to the molecule. We performed the averaging as in ref 28. The initial density operator, $\hat{\rho}^{ens}(0)$, of the resulting ensemble is given by summing over the pure states defined by the M = 8000 orientations:

$$\hat{\rho}^{ens}(0) = \frac{1}{M}\sum_{m=1}^{M} |\Psi_m(0)\rangle\langle\Psi_m(0)| \tag{8}$$

The initial density matrix on the basis of the $N_e = 3$ electronic states and N_g grid point can therefore be written as a quadratic form

$$\rho^{ens}(0) = \mathbf{A}\mathbf{A}^\dagger \tag{9}$$

where $\mathbf{A}$ is a rectangular matrix of dimensions $(N_e \times N_g = N_T) \times M$ made of M column vectors for each sampled orientation, $\mathbf{c}_m$, of N_T c_{ig}^m complex amplitudes. Since we compute $N_g = 26864$ grid points per electronic state, $N_T \gg M$. We showed in ref 28 that one can find the principal components of the matrix rectangular $\mathbf{A}$ by singular value decomposition:

$$\mathbf{A} = \mathbf{U}\Sigma\mathbf{V}^\dagger \tag{10}$$

The matrix $\sum$ is the diagonal matrix of the M nonzero eigenvalues of $\mathbf{A}$. $\mathbf{U}$ is a $N_T \times M$ matrix whose columns are the left eigenvectors of $\mathbf{A}$ that correspond to nonzero eigenvalues. The $M \times M$ matrix $\mathbf{V}$ is the matrix whose columns correspond to the M right eigenvectors of $\mathbf{A}$. One also shows that the matrix $\rho^{ens}(0)$ is rank deficient and has at most M nonzero eigenvalues with eigenvectors given by $\mathbf{U}_s$. We can therefore exactly rewrite $\rho^{ens}(0)$ is a sum of M "pure states" which are its principal components:

$$\rho^{ens}(0) = \mathbf{U}\Sigma\mathbf{V}^\dagger\mathbf{V}\Sigma\mathbf{U}^\dagger = \mathbf{U}\Sigma^2\mathbf{U}^\dagger = \sum_{s=1}^{M}\omega_s^2\mathbf{U}_s\mathbf{U}_s^\dagger \tag{11}$$

To compute the average dynamics, it is therefore strictly equivalent to solve the time-dependent Schrödinger equation for the M $\mathbf{U}_s$ vectors or for the M $\mathbf{c}_m$ ones. However, if the $\mathbf{A}$ matrix has a number of eigenvalues L that are much larger than the rest of them, we can approximately write its expansion (eq 11) in terms of L principal components $\mathbf{U}_s$, $L \ll M$:

$$\rho^{ens}(0) \approx \sum_{s=1}^{L}\omega_s^2\mathbf{U}_s\mathbf{U}_s^\dagger,\ L << M \tag{12}$$

In that case, propagating the L principal components leads to a considerable saving of computer time. In ref 28, we could show analytically that for initial states produced by sudden ionization, there were exactly $L = 3$ principal components of $\mathbf{A}$. In the case of initial amplitudes resulting from a sudden tunneling ionization process, we do not have such an analytical result because analytical dependence of the Keldysh tunneling ionization rates (eq 1) on the orientation of the field. However, the dynamics of the ensemble is recovered by three principal components which capture 99.97% of the trace of the ensemble density matrix for either one of the two isotopomers and for either of the two field strengths. More details are given in the SI.

We propagate the time-dependent Schrödinger equation using a finite difference algorithm for the kinetic energy and momentum operators for the three initial $\mathbf{U}_s$ vectors. The probabilities at each grid point are given by

$$P_{ig}(t) = \rho_{ig,ig}^{ens}(t) = \sum_{s=1}^{L} w_s |u_{ig}^s(t)|^2 \tag{13}$$

https://doi.org/10.1021/acs.jpca.1c06431
J. Phys. Chem. A XXXX, XXX, XXX−XXX

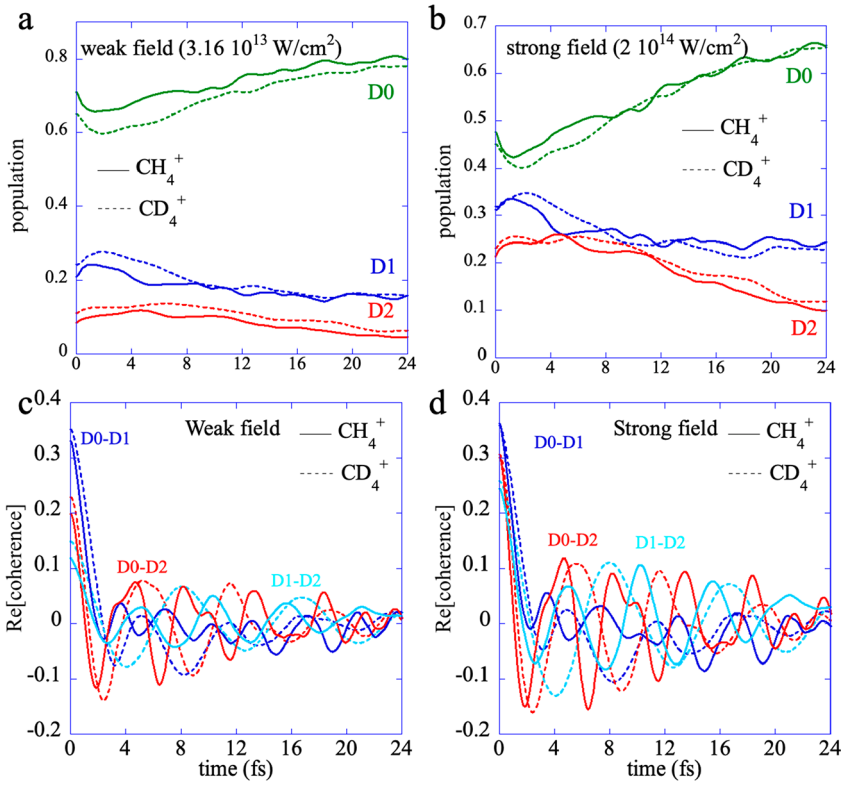

Figure 3. Panels a and b: Population dynamics, $P_i(t)$, for the ensemble of CH_4^+ (full lines) cations and CD_4^+ (dotted lines) upon tunneling ionization by a weak field (a) and a strong field (b). The population in D_0 is plotted in green, in D_1 in blue and in D_2 in red. Panels c and d: Electronic coherence dynamics (eq 16): (c) weak field, (d) strong field. The D_0-D_2 electronic coherence is plotted in red, the D_0-D_1 one in blue, and the D_1-D_2 coherence in azure.

where $u^s_{ig}(t)$ are the components of $\mathbf{U}_s(t)$ on the basis set and $w_s = \omega_s^2/\mathrm{Tr}[\rho(0)]$. The coherences terms of the ensemble density matrix take the form

$$\rho^{\mathrm{ens}}_{ig,jg'}(t) = \sum_{s=1}^{L} w_s u^s_{ig}(t) u^s_{jg'}(t) = \sum_{s=1}^{L} w_s \rho^s_{ig,jg'}(t) \tag{14}$$

where $\hat{\rho}^s(t) = |U_s\rangle\langle U_s|$ is the density matrix corresponding to its principal vector eigenvector $\mathbf{U}_s$.

The localization of the electronic coherence between electronic state i and j is diagonal in the grid index:

$$\rho^{\mathrm{ens}}_{ig,jg}(t) = \sum_{s=1}^{L} w_s u^s_{ig}(t) u^s_{jg}(t) = \sum_{s=1}^{L} w_s \rho^s_{ig,jg}(t) i \neq j \tag{15}$$

We report in the figures below the electronic coherences summed over all grid points

$$\rho^{\mathrm{ens}}_{ij}(t) = \sum_{g}^{N_g} \sum_{s=1}^{L} w_s u^s_{ig}(t) u^s_{jg}(t) = \sum_{g}^{N_g} \sum_{s=1}^{L} w_s \rho^s_{ig,jg}(t),\ i \neq j \tag{16}$$

The square modulus of the autocorrelation of the initial state takes the form:

$$\begin{aligned} |C(t)|^2 &= \mathrm{Tr}[\rho^{\mathrm{ens}}(0)\rho^{\mathrm{ens}}(t)] = \\ &\sum_{ig} \langle ig| \sum_{s} w_s |u_s(0)\rangle\langle u_s(0)| \sum_{jg'} |jg'\rangle\langle jg'| \sum_{s'} w_{s'} |u_{s'}(t)\rangle\langle u_{s'}(t)| ig\rangle \\ &= \sum_{ig} \sum_{jg'} \sum_{s} w_s u^s_{ig}(0) u^s_{jg'}(0)^* \sum_{s'} w_{s'}(0) u^{s'}_{jg'}(t) u^{s'}_{ig}{}^*(t) \\ &= \sum_{ig} \sum_{jg'} \left(\sum_{s} w_s \rho^s_{ig,jg'}(0) \right) \left(\sum_{s'} w_s \rho^{s'}_{jg',ig}(t) \right) \end{aligned} \tag{17}$$

So using eq 14, we see that

$$\begin{aligned} |C(t)|^2 &= Tr[\rho^{\mathrm{ens}}(0)\rho^{\mathrm{ens}}(t)] = \sum_{ig} \sum_{jg'} \rho^{\mathrm{ens}}_{ig,jg'}(0) \rho^{\mathrm{ens}}_{ig,jg'}{}^*(t) \\ &= \sum_{ig} \rho^{\mathrm{ens}}_{ig,ig}(0) \rho^{\mathrm{ens}}_{ig,ig}{}^*(t) + \sum_{i} \sum_{g' \neq g} \rho^{\mathrm{ens}}_{ig,ig'}(0) \rho^{\mathrm{ens}}_{ig,ig'}{}^*(t) \\ &\quad + \sum_{i \neq j} \sum_{g',g} \rho^{\mathrm{ens}}_{ig,jg'}(0) \rho^{\mathrm{ens}}_{ig,jg'}{}^*(t) \end{aligned} \tag{18}$$

is a direct probe of the electronic coherences (last term in eq 18). The second term corresponds to vibrational coherences on the same electronic state. Since the yield in harmonics is proportional to $|C(t)|^2$,[27] the harmonic yield is an experimental probe of electronic coherences.

3. RESULTS AND DISCUSSION

3.1. Population and Electronic Coherences Dynamics on the Nuclear Time Scale. The time evolution of the

https://doi.org/10.1021/acs.jpca.1c06431
J. Phys. Chem. A XXXX, XXX, XXX−XXX

probabilities of each electronic state, $P_i(t) = \sum_{g=1}^{N_g} P_{ig}(t)$, was computed using eq 13 for tunneling initial states resulting from tunnel ionization by the weak field (Figure 3a) and by the strong field pulse (Figure 3b) for the two isotopomers.

One can see from Figure 3 that the weak field strength (0.03 au, 3.16×10^{13} W/cm^2) pulse preferentially ionizes the ground state D_0 (initial populations on D_0 are 0.71 for CH_4^+ and 0.65 for CD_4^+). The initial population in D_1 is 0.21 for CH_4^+ and 0.24 for CD_4^+, about the double of that of D_2 (0.08 for CH_4^+ and 0.11 for CD_4^+). On the other hand, as discussed in section 2.2 above, the populations in D_1 and D_2 are larger for a tunnel ionization with the stronger pulse of 0.075 au (2×10^{14} W/cm^2): 0.31 for CH_4^+ and 0.32 for CD_4^+ in D_1, 0.21 for CH_4^+ and 0.23 for CD_4^+ in D_2, and 0.48 for CH_4^+ and 0.45 for CD_4^+ for D_0. The tunneling ionization process creates a superposition of states for each orientation of the electric field which leads to electronic coherences at the level of the ensemble. The electronic coherences summed over all grid points, eq 16, are plotted in panels c and d of Figure 3. The oscillations in the populations are due to the nonadiabatic transfers that are driven by the nuclear motion. One can see that the maximum of the oscillations of the population transfer coincide with large amplitudes of the oscillations of the electronic coherences. This is particularly clear at short time and for the oscillations of the D_0-D_2 electronic coherence. One also notices that oscillations of the electronic coherences in CD_4^+ are slower than in CH_4^+ and have a larger amplitude for the strong field initial states because there are more initial populations in the D_2 and the D_1 states. The oscillations of the electronic coherences are not periodic because of the strong NAC between the electronic states and the fact that the energy difference between the adiabatic electronic states varies rapidly in the FC region, see Figure 1. The coherences between the D_2 and the two lower states D_0 and D_1 are sustained by the NAC as long as there is population in the D_2 state because the latter is trapped around the T_d point on the steep D_2 potential. However, the wave packets on D_1 and D_0 are moving faster out of the T_d region because of the steep gradient of the PES around T_d.

3.2. Population and Electronic Coherences Dynamics on the Electronic Time Scale. The short time behavior up to 2 fs of the populations in the three electronic states and the electronic coherences (eq 16) are shown in Figure 4 for the weak field (Figure 4a) and the strong field (Figure 4b) initial states and the two isotopomers. Even on the short time (1.6 fs) probed by high harmonic spectroscopy using an 800 nm IR pulse,[20,21] the populations in each electronic state start to vary since the initial state of the cation is localized around the T_d point, where there is a strong nonadiabatic coupling. The isotope effect on the populations is not very large. On the other hand, the periods of the oscillations of the electronic coherences are strongly affected by the isotopic substitution as shown in Figure 4c for the weak field initial state and in Figure 4d for the strong one. One can see as expected that the dynamics of the D_0-D_1 coherence is not very much affected by the initial state while that of D_0-D_2 and D_1-D_2 coherence differ more because in the strong field case there is a larger amount of population initially present in D_2.

We compare in Figures 4e and 4f the time evolution of the electronic coherences for weak and strong field for CH_4^+ and CD_4^+ respectively. The onset of the differences in the dynamics of the electronic coherences occurs earlier for CH_4^+ than for

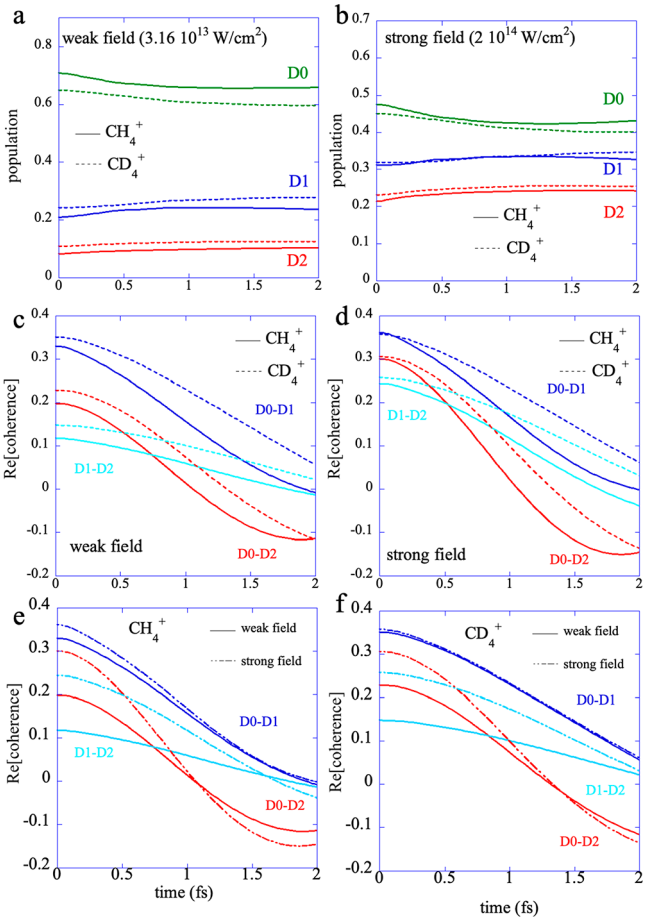

Figure 4. Panels a, b, c, d: same as Figure 3 for the short time range 0 to 2 fs. One can see that the D_0-D_1 coherence is not much affected by the localization of the initial state and the initial population in the D_2 state while the D_2-D_0 and D_1-D_2 coherences are very much affected. Panels e and f: Comparison of the time evolution of the electronic coherences at weak and strong field for CH_4^+ (e) and CD_4^+ (f). Here too, the biggest differences are for the D_2-D_0 and D_1-D_2 coherences.

CD_4^+. In this short time range, the nuclei have hardly time to move. We show in section 3 below that the difference is mainly due to the difference in the magnitude of amplitude transfers due to the nonadiabatic couplings, in particular for the D_1-D_2 electronic coherence. The comparison for the longer time dynamics is shown in Figure S2. One can see that the oscillations of the electronic coherences are getting slightly out of phase for the two field strengths as the dynamics unfolds, which is a manifestation of the effect of the amplitude transfers due to the NAC that involve the D_2 state that is accessed for the strong field ionization. This effect is larger for CH_4^+ than for CD_4^+.

We next show in Figure 5a the auto correlation functions (eq 17) of CH_4^+ and CD_4^+ computed including the NAC term in the Hamiltonian (eq 5) and in Figure 5b the autocorrelations computed without including the NAC terms. Their ratio are shown in Figure 5c and d, respectively. In the case of the exact dynamics computed for the strong field initial state, Figure 5c, we obtain a ratio of the autocorrelation functions, $|C(t)|_D^2/|C(t)|_H^2$ equal to ≈1.35 at 1 fs and 2.4 at 1.6 fs, in very good agreement with ref 20. In the interval 1 to 1.6 fs, the computed ratio for the low field strength initial state varies between 1.2 and 1.6. The large ratio of 2.4 computed for

https://doi.org/10.1021/acs.jpca.1c06431
J. Phys. Chem. A XXXX, XXX, XXX−XXX

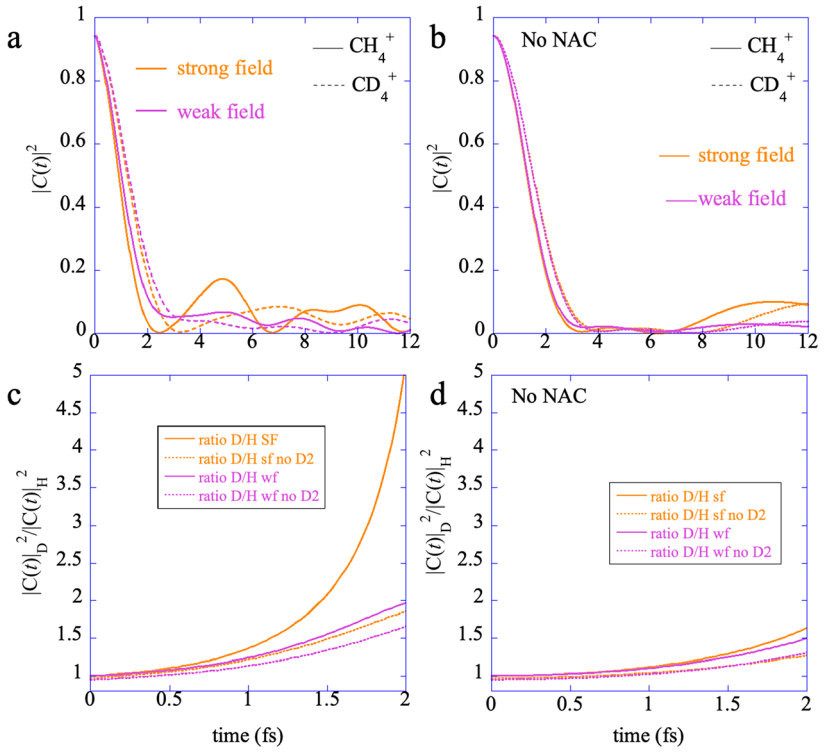

Figure 5. (a) Autocorrelation functions, $|C(t)|^2$ (eq 17), of the weak field, (violet) and strong field (orange) initial states for CH_4^+ (full lines) and CD_4^+ (dashes). (b) Autocorrelation functions of the initial state without including the NAC term in the Hamiltonian for computing the dynamics. (c) Ratio of the autocorrelation functions, $|C(t)|_D^2/|C(t)|_H^2$, computed exactly (full lines) and without the coherent terms involving the D_2 states (dots). (d) Ratio of the autocorrelation functions computed without the NAC term in the Hamiltonian.

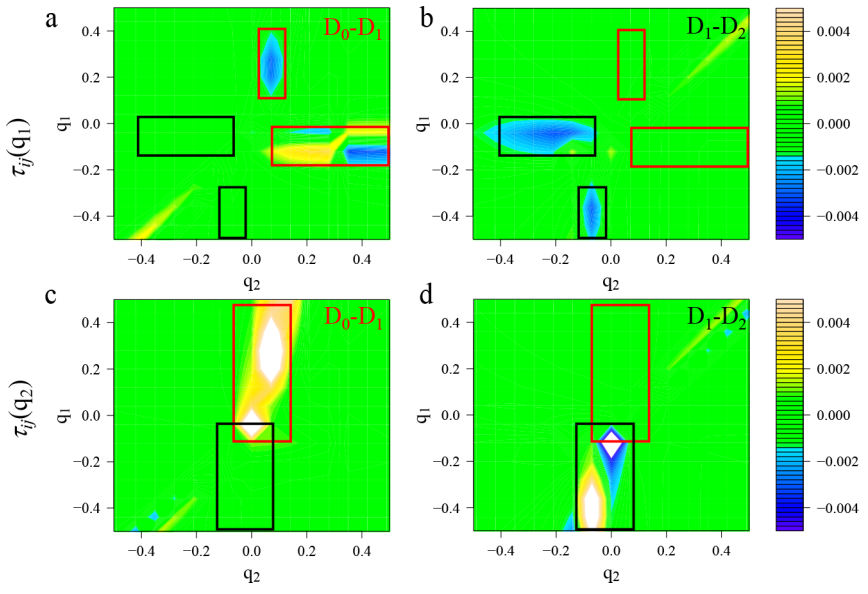

Figure 6. Regions of strong nonadiabatic coupling in CH_4^+ shown for the pairs of electronic states: (a, c) D_0-D_1 and (b, d) D_1-D_2. The transfer is due to derivative coupling along the q_1, panels (a, b) coordinate and along the q_2 one, panels (c, d). The regions of strong transfer are highlighted in rectangles for the D_0-D_1 (red color) and D_1-D_2 (black color). The resulting population flow is localized at specific zones in phase-space. For example, the red zone in panel c (D_0-D_1 NAC along q_2) is not at the same geometry as the red zone in panel d (D_1-D_2 NAC). But the red zone in panel c does appear as a higher coupling zone in panel a (D_0-D_1 NAC). The black zone in panel d is seen also in panel b, etc.

the high field strength initial state at 1.6 fs is due to the interplay between the electronic coherences that involve the D_2 state and the onset of nonadiabatic interactions as the nuclei start to move. On the other hand, the ratio $|C(t)|_D^2/|C(t)|_H^2 = 1.6$ computed for the low field strength initial state is essentially due to the isotope effect due to the D_0-D_1 coherence. This value is smaller but close to the ratio of 1.86 that one expects on the basis of the ratio of the effective masses of the C−D and C−H bonds. When the terms that involve the electronic coherences D_2-D_0 and D_2-D_1 in the last term of eq 18 are not included in the computation of the autocorrelation functions, dotted lines in Figure 5c, the ratio

https://doi.org/10.1021/acs.jpca.1c06431
J. Phys. Chem. A XXXX, XXX, XXX−XXX

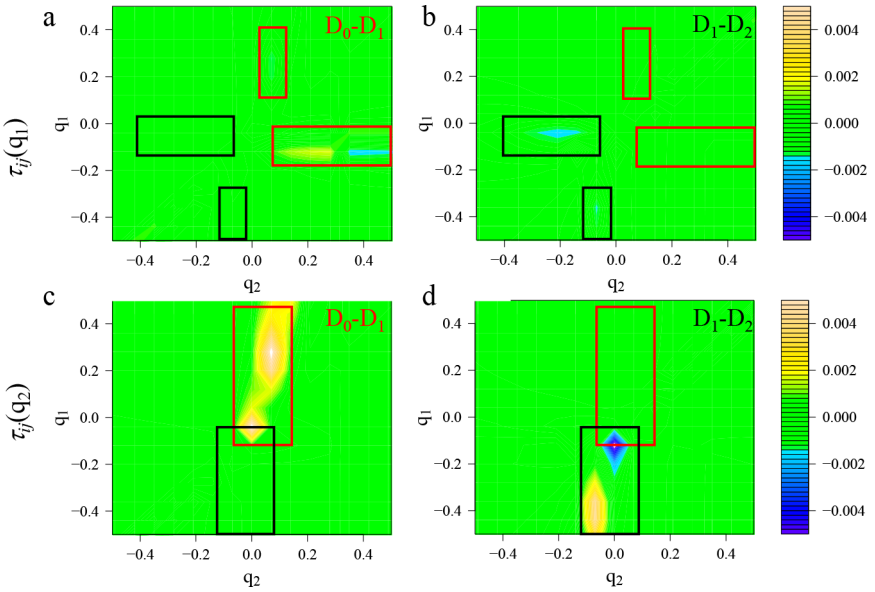

Figure 7. Regions of strong nonadiabatic coupling in CD_4^+ shown for pairs of electronic states: (a, c) D_0−D_1 and (b, d) D_1−D_2. The derivative coupling with respect to q_1, panels a, b, is weaker in CD_4^+ as compared with CH_4^+. For more details see the caption of the Figure 6.

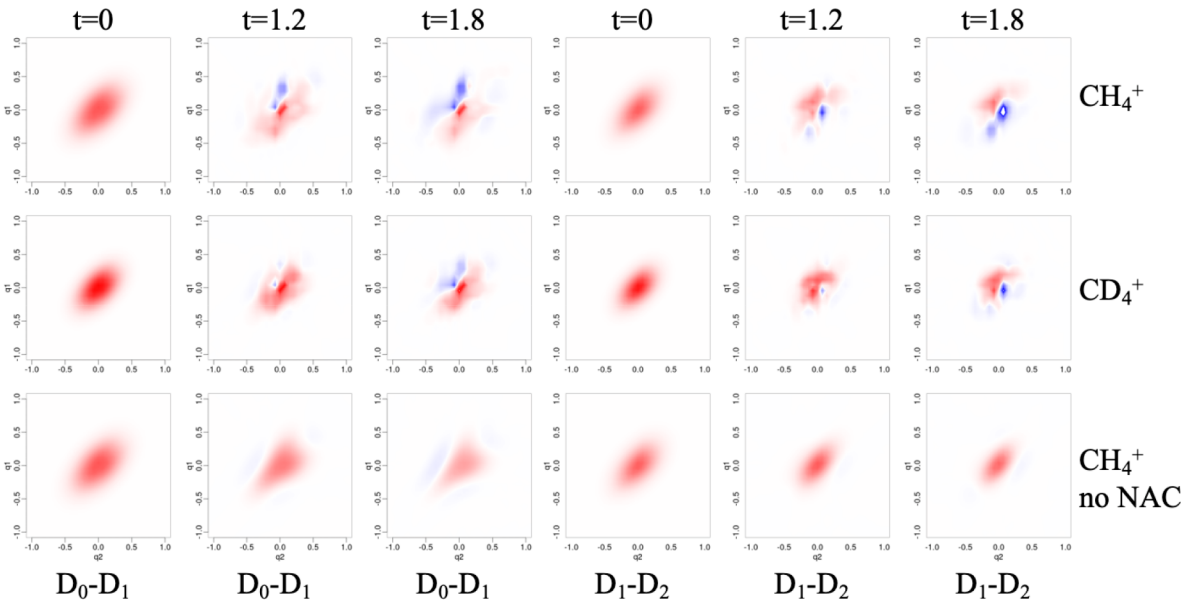

Figure 8. Heatmaps of the dynamics of the localization of the real part of electronic coherences, D_0−D_1 and D_2−D_1 at every grid point for the strong field case, computed for CH_4^+ (top row), CD_4^+ (middle row) and CH_4^+ without including the NAC term in the Hamiltonian (bottom row). The time is in fs.

$|C(t)|_D^2/|C(t)|_H^2$ is similar for the high and low field initial states and has a lower value. At 1.6 fs, it is equal to ≈1.6 for the strong field initial state and to 1.4 for weak field one. The effect of the NAC is further seen by comparing Figure 5a and 5c with Figure 5b and 5d which are computed without including the NAC term in the Hamiltonian, eq 5. In that case, the ratio for strong and weak field initial states at 1.6 fs is ≈1.3 and it is 1.15 when the coherence terms due to the D_2 are not included in the dynamics.

3.3. Role of Nonadiabatic Coupling in the Strong Isotope Effect. The results presented in section 3.2 point to a dominant role of the interplay between the electronic coherences and the nonadiabatic coupling in getting an isotope effect different from that expected in the basis of the effective mass ratios. The computed ratio of the masses in the kinetic energy term and in the NAC term in the Hamiltonian is ≈2. In order to get a better understanding on the role of the NAC terms, we show heatmaps of the localization of the two components of the NAC vectors (eq S6), $\tau_{ij}(q_1)$ and $\tau_{ij}(q_2)$, at each grid point in the Franck−Condon region for CH_4^+ in Figure 6 and CD_4^+ in Figure 7 for the pairs of electronic states (D_2, D_1) and (D_1, D_0). The heatmap for the full range of the grid and the three pairs of electronic states is shown for CH_4^+ in Figure S3. One can see from Figure S3 that the D_0−D_2 NAC values on the grid are 50 times smaller than those of D_0−D_1 and D_1−D_2. In the Franck−Condon region the seams of the NAC exhibit different localization for the D_0−D_1 and D_1−D_2 coupling. The D_0−D_1 coupling is localized toward the positive

https://doi.org/10.1021/acs.jpca.1c06431
J. Phys. Chem. A XXXX, XXX, XXX−XXX

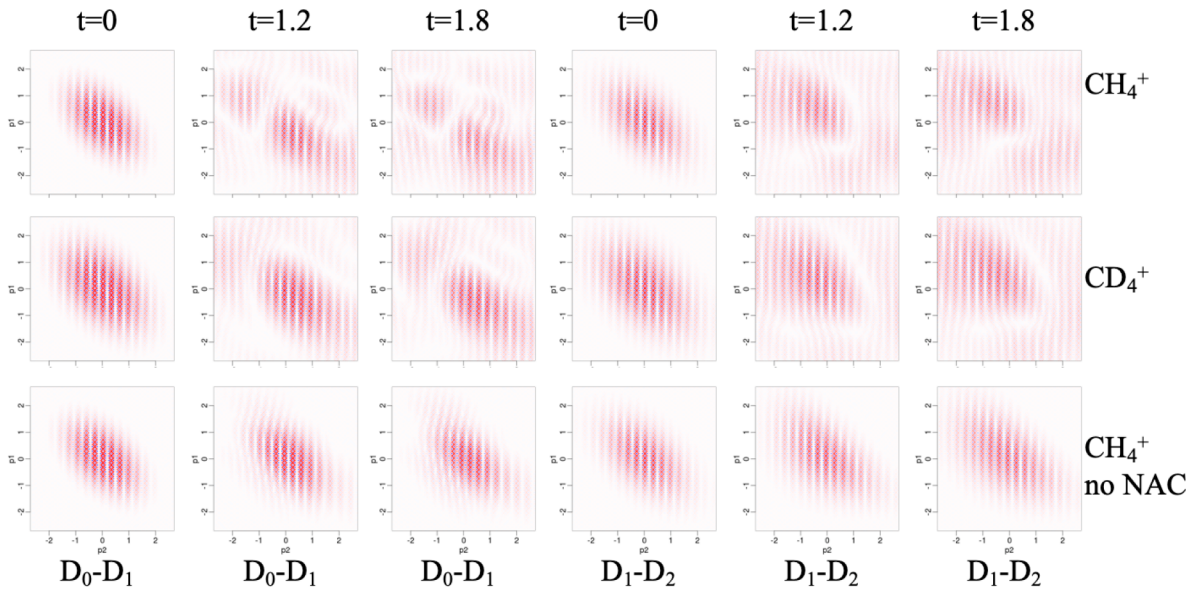

Figure 9. Heatmaps of the dynamics of the localization of the real part of electronic coherences, D_0-D_1 and D_2-D_1 in momentum space for the strong field case, computed for CH_4^+ (top row), CD_4^+ (middle row) and CH_4^+ without including the NAC term in the Hamiltonian (bottom row).

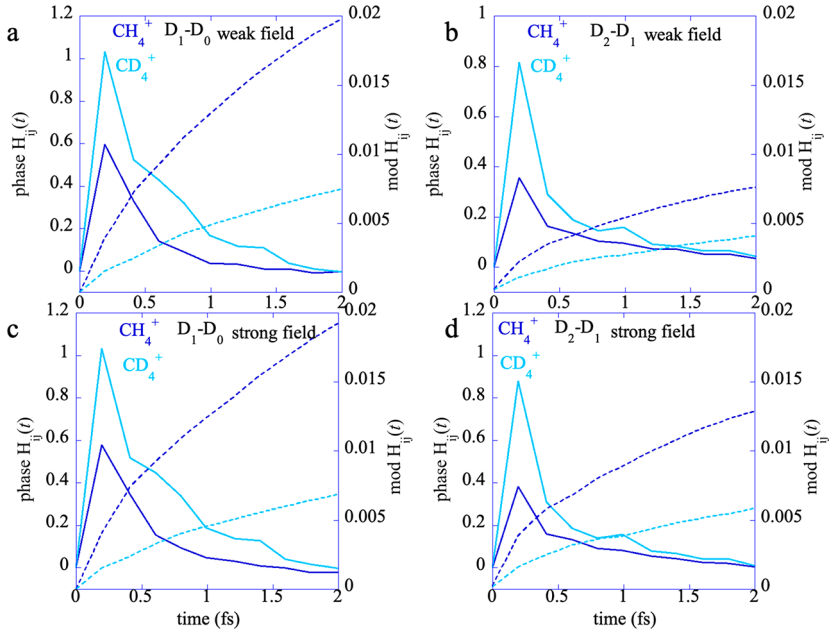

Figure 10. Early time evolution of the phases (left ordinate axis, full lines) and moduli (right ordinate axis, dashes) of NAC term $H_{ij}(t)$, eq 7, computed for the q_2 component of the NAC vector for the weak field (panel a: term D_1-D_0; panel b: term D_2-D_1) and strong field (panel c: term D_1-D_0; panel d: term D_2-D_1) initial states for the two isotopomers (CH_4^+ blue and CD_4^+ in azure).

values of the (q_1, q_2) coordinates, while D_1-D_2 primarily couples toward the negative values of the (q_1, q_2). This localization induces an amplitude flow that is localized at specific zones in phase-space. This flow leads to the rapid reorganization of the population in all three electronic states (Movies S1−S4 in the SI) in the first 2 fs of the dynamics, before the nuclei have time to significantly move.

The effect of the localized NAC coupling on the population is reflected in the heatmaps of the spatial localization of the electronic coherences D_0-D_1 and D_1-D_2, plotted in coordinate space in Figure 8 and in momentum space in Figure 9. The top row of Figures 8 and 9 is plotted for CH_4^+, the middle row CD_4^+, and bottom row is for CH_4^+, computed without including the NAC term in the Hamiltonian (eq 5). The patterns that develop as a function of time in the first 2 fs follow the patterns of the localization of the components of the NAC vector shown in Figures 6 and 7 above. They are slower to develop for CD_4^+ than for CH_4^+ as already seen in Figure 4 for the dynamics of the populations and the coherences integrated over the grid. In the bottom row of Figure 8, computed for CH_4^+ without including the NAC term, one sees that the localization of the electronic coherences hardly changes during the first 2 fs because the wave packets have hardly moved. This can be verified from the movies of the localization of the wave packets on D_0, D_1, and D_2 computed with and without NAC for the two isotopomers (see SI).

In momentum space (Figure 9), the fast oscillations are due to the overall size of the coherence in space and they are

https://doi.org/10.1021/acs.jpca.1c06431
J. Phys. Chem. A XXXX, XXX, XXX−XXX

slightly slower for CD_4^+ than for CH_4^+. The development of smaller patterns that oscillates slower in the momentum coherence maps results from the fragmentation of the electronic coherences due to the localization of the NAC terms in the Hamiltonian shown in Figures 6 and 7.

The oscillating patterns of the electronic coherences in space and in momentum before the nuclei start to move are a manifestation of a purely electronic time scale due to the NAC coupling. They result from the interplay between the localization in space of the NAC seams shown in Figures 6 and 7. Since the NAC terms, $\tau_{ij}(g)$, exhibit the expected ratio of ≈2 at every grid point, the strong nonclassical isotope effect in the ratio of the autocorrelation functions plotted in Figure 5 arises from the momentum factor in the NAC term of eq 5. The tunneling ionization process creates a coherent superposition of the states of the cation. When the NAC term acts on an already existing coherence between the two states that are coupled, the direction and the magnitude of the amplitude transfer depend on the phase of the electronic coherence. We showed in refs 30,31, for diatomic molecules using a Condon approximation[40] for the nonadiabatic coupling, that the transfer is maximum when the phase of the momentum overlap between the wave packet on each coupled electronic state, $\langle i|\hat{P}|j\rangle$, is stationary. On the grid, we have an exact Condon-like separation at each grid point (see the momentum factor in the NAC term of eq 5). In order to estimate the role of the phase of the electronic coherence in the efficiency of the transfer of amplitude between the two states for the two isotopomers, we use the value of the NAC coupling, $H_{ij}(t)$, averaged over grid points between the wave packets on the two states that are coupled, eq 7. Only the phases of the D_1-D_2 and D_0-D_1 coherences become stationary between 1 and 2 fs, and this is only for the q_2 components of the NAC vector τ_{ij}. Their values are plotted in Figure 10. The plots of the values of $H_{ij}(t)$ for the other coherences are given in Figure S4 of the SI. The values of the phase and the modulus of $H_{10}(t)$ and $H_{21}(t)$ are plotted for the weak field initial state in panels a and b, respectively, of Figure 10 and in Figure 10c,d for the strong field case. One can see from Figure 10 that the phases of $H_{ij}(t)$ become stationary at earlier times for CH_4^+ than for CD_4^+ which explains the earlier onset of amplitude transfer for CH_4^+ between these two pairs of states. One also see that the modulus of the coupling term is significantly larger for the D_1-D_2 coherence for strong field initial state, which explains the important role played by this coherence in the nonclassical strong isotope effect observed on the ratio of the autocorrelation functions for the strong field initial state. Conversely, in the weak field case, one is getting an isotope effect smaller than expected from the mass ratio, which is essentially due to the D_0-D_1 electronic coherence. We note also that at short time, it is the component of the NAC vector along q_2 that is pointing to the secondary D_{2d} minimum on the grid that is dominant in the amplitude transfer. Movies of the rates of population transfer for the strong field initial state at each grid points are available in the SI.

4. CONCLUSIONS

We investigated the very early time dynamics of the two isotopomers of the methane cation obtained by strong field ionization of the neutral ground state. We showed that the tunneling ionization prepares a superposition of the three lowest states of the cation. Two field strengths were considered for the strong field tunnelling ionization process, a weaker field that effectively does not access the higher D_2 electronic state and a stronger one for which the D_2 is significantly populated. The prompt electronic dynamics that follows the strong field ionization process exhibits a strong isotope dependence with a ratio of 2.4 in the autocorrelation functions, in agreement with the high harmonic spectroscopy experimental results which involve a tunneling ionization process with the same field strength.[20,21] However, the dynamics for the weak field initial state leads to an isotope effect of 1.4 in the autocorrelation functions, which is smaller than the mass ratio. The magnitude of the effect is not changing upon averaging over the orientation of the electric field of the ionizing pulse with respect to the molecule. For both cases, we show that the isotope effect has a nonclassical origin and is due to the interplay between the dynamics of the electronic coherences and the amplitude transfers between each pair of electronic states because of the nonadiabatic coupling. This nonclassical isotope effect occurs on a purely electronic time scale, before a significant onset of nuclear motion. We generalized the analysis of the isotope effect for systems in a coherent superposition of states developed for diatomic molecules[29−32] to the present case of a 2D system, for which the NAC seams exhibit complex localization in space. We show by analyzing the phase and the modulus of the nonadiabatic coupling between each pair of states that the D_0-D_1 and the D_1-D_2 electronic coherences play a major role in the nonclassical isotope effect. These are the coherences for which the phase of the coupling term, becomes stationary, which is the condition for an efficient amplitude transfer.

■ ASSOCIATED CONTENT

Supporting Information

The Supporting Information is available free of charge at https://pubs.acs.org/doi/10.1021/acs.jpca.1c06431.

Additional details on the computational methodology and supplemental figures (PDF)

Video S1: Population dynamics in CH_4^+ for a weak field initial state (MP4)

Video S2: Population dynamics in CD_4^+ for a weak field initial state (MP4)

Video S3: Population dynamics in CH_4^+ for a strong field initial state (MP4)

Video S4: : Population dynamics in CD_4^+ for a strong field initial state (MP4)

Video S5: Population dynamics in CH_4^+ for a strong field initial state without NAC in the Hamiltonian (MP4)

Video S6: Population dynamics in CD_4^+ for a strong field initial state without NAC in the Hamiltonian (MP4)

Video S7: Rate of population transfer for CH_4^+ for a strong field initial state (MP4)

Video S8: Rate of population transfer for CD_4^+ for a strong field initial state (MP4)

■ AUTHOR INFORMATION

Corresponding Author

F. Remacle − *Theoretical Physical Chemistry, University of Liège, 4000 Liège, Belgium; The Fritz Haber Research Center for Molecular Dynamics, The Hebrew University of Jerusalem, 91904 Jerusalem, Israel;* orcid.org/0000-0001-7434-5245; Email: fremacle@uliege.be

https://doi.org/10.1021/acs.jpca.1c06431
J. Phys. Chem. A XXXX, XXX, XXX−XXX

Authors

Martin Blavier − *Theoretical Physical Chemistry, University of Liège, 4000 Liège, Belgium*

Ksenia Komarova − *The Fritz Haber Research Center for Molecular Dynamics, The Hebrew University of Jerusalem, 91904 Jerusalem, Israel*

Cayo E. M. Gonçalves − *Theoretical Physical Chemistry, University of Liège, 4000 Liège, Belgium*

R. D. Levine − *The Fritz Haber Research Center for Molecular Dynamics, The Hebrew University of Jerusalem, 91904 Jerusalem, Israel; Department of Chemistry and Biochemistry and Department of Molecular and Medical Pharmacology, David Geffen School of Medicine, University of California, Los Angeles, California 90095, United States*

Complete contact information is available at: https://pubs.acs.org/10.1021/acs.jpca.1c06431

Notes

The authors declare no competing financial interest.

■ ACKNOWLEDGMENTS

This work was supported by the Fonds National de la Recherche Scientifique (Belgium), F.R.S.-FNRS research grants #T.0132.16 and #J.0012.18. Computational resources have been provided by the Consortium des Equipements de Calcul Intensif (CECI), funded by the F.R.S.-FNRS under Grant # 2.5020.11. Support of the COST action Attochem(-CA18222) is also acknowledged. We thank Dr. Stephan van den Wildenberg for the computation of the Dyson orbitals of methane.

■ REFERENCES

(1) Corkum, P. B.; Krausz, F. Attosecond science. *Nat. Phys.* **2007**, *3*, 381−387.

(2) Krausz, F.; Ivanov, M. Attosecond physics. *Rev. Mod. Phys.* **2009**, *81*, 163−234.

(3) Goulielmakis, E.; Schultze, M.; Hofstetter, M.; Yakovlev, V. S.; Gagnon, J.; Uiberacker, M.; Aquila, A. L.; Gullikson, E. M.; Attwood, D. T.; Kienberger, R.; et al. Single-cycle nonlinear optics. *Science* **2008**, *320*, 1614−1617.

(4) Calegari, F.; Sansone, G.; Stagira, S.; Vozzi, C.; Nisoli, M. Advances in attosecond science. *J. Phys. B: At., Mol. Opt. Phys.* **2016**, *49*, 062001.

(5) Galli, M.; Wanie, V.; Lopes, D. P.; Månsson, E. P.; Trabattoni, A.; Colaizzi, L.; Saraswathula, K.; Cartella, A.; Frassetto, F.; Poletto, L.; et al. Generation of deep ultraviolet sub-2-fs pulses. *Opt. Lett.* **2019**, *44*, 1308−1311.

(6) Hernández-García, C.; Popmintchev, T.; Murnane, M. M.; Kapteyn, H. C.; Plaja, L.; Becker, A.; Jaron-Becker, A. Isolated broadband attosecond pulse generation with near- and mid-infrared driver pulses via time-gated phase matching. *Opt. Express* **2017**, *25*, 11855−11866.

(7) Nisoli, M.; Decleva, P.; Calegari, F.; Palacios, A.; Martín, F. Attosecond electron dynamics in molecules. *Chem. Rev.* **2017**, *117*, 10760−10825.

(8) Lepine, F.; Ivanov, M. Y.; Vrakking, M. J. J. Attosecond molecular dynamics: Fact or fiction? *Nat. Photonics* **2014**, *8*, 195−204.

(9) Vrakking, M. J. J.; Lepine, F. *Attosecond molecular dynamics*; The Royal Society of Chemistry: Cambridge, 2019; pp P001−500.

(10) Remacle, F.; Levine, R. D. An electronic time scale for chemistry. *Proc. Natl. Acad. Sci. U. S. A.* **2006**, *103*, 6793−6798.

(11) Muskatel, H. B.; Remacle, F.; Levine, R. D. The post born-oppenheimer regime: Dynamics of electronic motion in molecules by attosecond few cycle spectroscopy. *Phys. Scr.* **2009**, *80*, 048101−7.

(12) Signorell, R.; Merkt, F. Pfi-zeke photoelectron spectra of the methane cation and the dynamic jahn−teller effect. *Faraday Discuss.* **2000**, *115*, 205−228.

(13) Wörner, H. J.; van der Veen, R.; Merkt, F. Jahn-teller effect in the methane cation: Rovibronic structure and the geometric phase. *Phys. Rev. Lett.* **2006**, *97*, 173003.

(14) Knight, L. B.; Steadman, J.; Feller, D.; Davidson, E. R. Experimental evidence for a c2v (2b1) ground-state structure of the methane cation radical: Esr and ab initio ci investigations of methane cation radicals (ch4+ and cd2h2+) in neon matrixes at 4 k. *J. Am. Chem. Soc.* **1984**, *106*, 3700−3701.

(15) Knight, L. B.; King, G. M.; Petty, J. T.; Matsushita, M.; Momose, T.; Shida, T. Electron spin resonance studies of the methane radical cations (12,13ch+4, 12,13cdh+3, 12cd2h+2, 12cd3h+, 12 cd +4) in solid neon matrices between 2.5 and 11 k: Analysis of tunneling. *J. Chem. Phys.* **1995**, *103*, 3377−3385.

(16) Paddon-Row, M. N.; Fox, D. J.; Pople, J. A.; Houk, K. N.; Pratt, D. W. Dynamic jahn-teller effect in methane radical cation. Location of the transition structures for hydrogen scrambling and inversion. *J. Am. Chem. Soc.* **1985**, *107*, 7696−7700.

(17) Opalka, D.; Domcke, W. High-order expansion of t2 × t2 jahn−teller potential-energy surfaces in tetrahedral molecules. *J. Chem. Phys.* **2010**, *132*, 154108.

(18) Frey, R. F.; Davidson, E. R. Potential energy surfaces of ch+4. *J. Chem. Phys.* **1988**, *88*, 1775−1785.

(19) Jacovella, U.; Wörner, H. J.; Merkt, F. Jahn-teller effect and large-amplitude motion in ch4+ studied by high-resolution photoelectron spectroscopy of ch4. *J. Mol. Spectrosc.* **2018**, *343*, 62−75.

(20) Baker, S.; Robinson, J. S.; Haworth, C. A.; Teng, H.; Smith, R. A.; Chirilă, C. C.; Lein, M.; Tisch, J. W. G.; Marangos, J. P. Probing proton dynamics in molecules on an attosecond time scale. *Science* **2006**, *312*, 424.

(21) Marangos, J. P.; Baker, S.; Kajumba, N.; Robinson, J. S.; Tisch, J. W. G.; Torres, R. Dynamic imaging of molecules using high order harmonic generation. *Phys. Chem. Chem. Phys.* **2008**, *10*, 35−48.

(22) Patchkovskii, S. Nuclear dynamics in polyatomic molecules and high-order harmonic generation. *Phys. Rev. Lett.* **2009**, *102*, 253602.

(23) Madsen, C. B.; Abu-samha, M.; Madsen, L. B. High-order harmonic generation from polyatomic molecules including nuclear motion and a nuclear modes analysis. *Phys. Rev. A: At., Mol., Opt. Phys.* **2010**, *81*, 043413.

(24) Mondal, T.; Varandas, A. J. C. The jahn-teller effect in the triply degenerate electronic state of methane radical cation. *J. Chem. Phys.* **2011**, *135*, 174304.

(25) Mondal, T.; Varandas, A. J. C. On extracting subfemtosecond data from femtosecond quantum dynamics calculations: The methane cation. *J. Chem. Theory Comput.* **2014**, *10*, 3606−3616.

(26) Mondal, T.; Varandas, A. J. C. Structural evolution of the methane cation in subfemtosecond photodynamics. *J. Chem. Phys.* **2015**, *143*, 014304.

(27) Lein, M. Attosecond probing of vibrational dynamics with high-harmonic generation. *Phys. Rev. Lett.* **2005**, *94*, 053004.

(28) Gonçalves, C. E. M.; Levine, R. D.; Remacle, F. Ultrafast geometrical reorganization of a methane cation upon sudden ionization: An isotope effect on electronic non-equilibrium quantum dynamics. *Phys. Chem. Chem. Phys.* **2021**, *23*, 12051−12059.

(29) Ajay, J. S.; Komarova, K. G.; Remacle, F.; Levine, R. D. Time-dependent view of an isotope effect in electron-nuclear non-equilibrium dynamics with applications to n2. *Proc. Natl. Acad. Sci. U. S. A.* **2018**, *115*, 5890−5895.

(30) Komarova, K.; vandenWildenberg, S.; Remacle, F.; Levine, R. D. Correlated electron-nuclear motion during non-adiabatic transitions in lih and its isotopomers. *J. Phys. B: At., Mol. Opt. Phys.* **2020**, *53*, 134001.

(31) Komarova, K. G.; Remacle, F.; Levine, R. D. Time resolved mechanism of the isotope selectivity in the ultrafast light induced dissociation in n2. *J. Chem. Phys.* **2019**, *151*, 114308.

(32) Komarova, K.; Remacle, F.; Levine, R. D. The density matrix via few dominant observables: The quantum interference in the isotope effect for atto-pumped n2. *J. Chem. Phys.* **2021**, *155*, 024109.
(33) Werner, H.-J.; Knowles, P. J.; Knizia, G.; Manby, F. R.; Schütz, M. Molpro: A general-purpose quantum chemistry program package. *Wiley Interdisciplinary Reviews: Computational Molecular Science* **2012**, *2*, 242−253.
(34) Corkum, P. B. Plasma perspective on strong field multiphoton ionization. *Phys. Rev. Lett.* **1993**, *71*, 1994−1997.
(35) Zhao, S.-F.; Xu, J.; Jin, C.; Le, A.-T.; Lin, C. D. Effect of orbital symmetry on the orientation dependence of strong field tunnelling ionization of nonlinear polyatomic molecules. *J. Phys. B: At., Mol. Opt. Phys.* **2011**, *44*, 035601.
(36) Tong, X. M.; Zhao, Z. X.; Lin, C. D. Theory of molecular tunneling ionization. *Phys. Rev. A: At., Mol., Opt. Phys.* **2002**, *66*, 033402.
(37) Ortiz, J. V. Dyson-orbital concepts for description of electrons in molecules. *J. Chem. Phys.* **2020**, *153*, 070902.
(38) Spanner, M.; Patchkovskii, S.; Zhou, C.; Matsika, S.; Kotur, M.; Weinacht, T. C. Dyson norms in xuv and strong-field ionization of polyatomics: Cytosine and uracil. *Phys. Rev. A: At., Mol., Opt. Phys.* **2012**, *86*, 053406.
(39) van den Wildenberg, S.; Mignolet, B.; Levine, R. D.; Remacle, F. Temporal and spatially resolved imaging of the correlated nuclear-electronic dynamics and of the ionized photoelectron in a coherently electronically highly excited vibrating lih molecule. *J. Chem. Phys.* **2019**, *151*, 134310.
(40) Condon, E. U. The franck-condon principle and related topics. *Am. J. Phys.* **1947**, *15*, 365−374.

https://doi.org/10.1021/acs.jpca.1c06431
J. Phys. Chem. A XXXX, XXX, XXX−XXX